JOM, Vol. 75, No. 8, 2023
https://doi.org/10.1007/s11837-023-05902-7

Microstructure Evolution and Tensile Properties of Forged Mg-Zn-Zr Alloys: Effects of Zr Microalloying

GUANG ZENG,[1] HU YAO,[1] WEI SUN,[1] HONGYI ZHAN,[2,4] CONGJIE WANG,[2] JIANFENG WANG,[2] LIXIN HUANG,[3,5] MENG LI,[3] and JINGRU SHEN[3]

1.—School of Materials Science and Engineering, Central South University, Changsha 410083, China. 2.—China Science Lab, General Motors Global Research and Development, Shanghai 201206, China. 3.—CITIC Dicastal Co. Ltd., Qinhuangdao 066000, China. 4.—e-mail: henry.zhan@gm.com. 5.—e-mail: huanglixin@dicastal.com

Mg-Zn-Zr wrought alloys have been widely developed for lightweight applications. Zr microalloying contributes to remarkable grain refinement during solidification and bimodal microstructure via forging. To obtain an optimum Zr content for a balance between cost and mechanical property, it is necessary to understand the influence of varied Zr addition levels on the microstructure and mechanical property of the final forged product. In the present study, two levels of Zr addition (nominally 0.40 wt.% and 0.60 wt.%) were added to a Mg-3 wt.% Zn alloy to investigate the effect of varied Zr contents on the microstructures under as-cast, as-forged and tensile-strained conditions, as well as the uniaxial tensile properties of the as-forged alloy. The as-forged microstructures comprise fine dynamic recrystallized (DRXed) grains and coarse deformed (unDRXed) domains, which become more refined with the Zr content increasing from $\sim$ 0.43 wt.% to $\sim$ 0.67 wt.%. The microstructural change caused by the increased Zr addition has minor impact on 0.2% proof stress but remarkably improves both uniform and post-uniform elongations, for which the underlying mechanisms have been discussed.

INTRODUCTION

The original function of adding zirconium (Zr) into magnesium (Mg) is to refine grain size of as-cast microstructure. Previous studies have revealed that α-Zr particles can act as heterogeneous nucleation substrate for α-Mg grain and Zr solute has a strong restricting effect on the growth of α-Mg grain,[1–4] both contributing to remarkable grain refinement. Since Zr has a strong tendency to react with some elements such as Al, Si and Mn to form intermetallic compounds (IMCs), the grain refinement effect of Zr addition will be poisoned in the commonly used Mg-Al-Zn, Mg-Al-Mn, Mg-Al-Si alloys.[1] In contrast, zinc (Zn) and rare earth (RE) elements such as La, Ce and Gd are compatible with Zr. Hence, Mg alloys with Zr, Zn and/or RE as major microalloying elements have been developed.[5,6] Among them, Mg-Zn-Zr alloys, such as ZK30 and ZK60, are the commercially available Zr-containing Mg wrought alloys which have been widely studied for applications in the biomedical, aerospace and automotive industries.[7–15]

The microalloying of Zr is normally carried out via adding Mg-Zr master alloy into Mg melt.[4] Due to the large difference in the densities of Zr and Mg (ρ_{Mg} = 1.72 g/cm^3 versus ρ_{Zr} = 6.54 g/cm^3), a considerable portion of α-Zr particles released from Mg-Zr master alloy tends to settle to the bottom of holding furnace resulting in a loss of Zr.[16–19] Therefore, to satisfy a required Zr content, an excess amount of Mg-Zr master alloy needs to be added. As Zr is much more expensive than Mg, this adds to the production cost of Mg-Zn-Zr alloys. Moreover, solute Zr content (Zr_s) in the Mg matrix decreased remarkably after remelting, which

(Received February 7, 2023; accepted May 10, 2023; published online May 24, 2023)

implies that Zr cannot be recycled by remelting Mg-Zn-Zr alloy scraps.[20] Therefore, it is necessary to understand the effects of varied Zr addition levels on the microstructure and mechanical properties of Mg-Zn-Zr alloys and optimize Zr content to reduce the waste of Zr. To refine the grain size of as-cast microstructure to < 100 μm, the total Zr content (Zr_t) added to Mg-Zn-Zr alloys was generally > 0.5 wt.% (all compositions quoted afterwards are in weight percent unless otherwise stated).[4,21] With Zr_t further increased, grain refinement effect did not show remarkable improvement. It is reported that the grain refinement effect was associated with Zr addition saturated at Zr_t of $\sim 0.6\%$.[5,22]

In addition to the grain refinement effect, Zr addition resulted in the formation of Zr-rich coring structures in the as-cast microstructure,[23,24] and nano-sized Zr-containing particles precipitated out in the Zr-rich cores during homogenization heat treatment and hot forming processes.[25–27] The formed Zr-containing precipitates impeded dynamic recrystallization (DRX) behavior via pinning on dislocations and sub-grain boundaries.[28,29] As a result, bimodal microstructure with coarse unDRXed domains dispersed in refined DRXed grains has been widely reported in the Zr-containing Mg alloys after hot deformations.[26,30,31] Oh-ishi et al.[31] added 0.6% Zr into a Mg-Zn-Ag-Ca alloy and reported that the obtained bimodal microstructure after a hot extrusion at 350 °C exhibited a significantly higher strength relative to the counterpart without Zr addition. Bhattacharjee et al.[32] observed a similar phenomenon when adding 0.6% Zr into a Mg-6%Zn alloy and reported that the tensile yield strength of extruded Mg-6%Zn alloy was increased from 162 MPa to 254 MPa with the Zr addition. Though past work has shown beneficial impact of Zr addition on strength property, it is still of great interest to further explore the effects of varied levels of Zr addition on the microstructure and mechanical properties of hot-formed Mg-Zn-Zr alloys in a systematic comparative study.

Mg-Zn-Zr alloys have attracted great interest from the automotive industry for lightweight applications due to their extraordinary plastic deformability, excellent corrosion resistance and moderate strength property after hot forming.[9,26,33,34] In the present study, two levels of Zr addition (0.40% and 0.60% in nominal) were added to a Mg-3%Zn alloy to evaluate the effects of varied levels of Zr addition on the microstructure and tensile property of as-forged Mg-Zn-Zr alloy. As-cast, as-forged and tensile-strained microstructures were characterized in detail for understanding the microstructure-property relationship, as affected by varied levels of Zr addition.

EXPERIMENTAL PROCEDURES

Billet Casting

Two levels of Zr addition have been designed for a Mg-3%Zn-Zr alloy. The alloy with a nominal Zr content of 0.4% is designated as 'low Zr,' while the other alloy with a nominal Zr content of 0.6% is designated as 'high Zr.' Direct-chill (DC) casting of Mg-Zn-Zr alloy billets was conducted in the plant of Gonleer Co., Ltd. (Datong, Shanxi Province, China). The melting of pure Mg and pure Zn wafers was carried out in a resistance furnace at 740–760 °C under the protection of a mixed atmosphere of CO_2 and SF_6. The first round of refining was conducted by introducing refining agent ($38 \pm 3\%$ $MgCl_2$, $37 \pm 3\%$ KCl, $10 \pm 3\%$ NaCl, $5 \pm 1\%$ $CaCl_2$ and $9 \pm 3\%$ $BaCl_2$) into the melt and conducting mechanical stirring with a frequency of 22–24 Hz for 5 min. Mg-30%Zr master alloy was then added to the melt, and its dosage was based on the supplier's experience that the yield rate of Zr is $\sim 40\%$. The second round of refining was conducted after the addition of Mg-30%Zr master alloy, followed by a 30-min standing. The composition of the melt was measured by spark optical emission spectrum (OES) method on site. After the alloy chemistry satisfied the requirement, the casting began. The melt was transferred to a mold at ~ 730 °C and cast into a log with a diameter of 400 mm, at an average casting velocity of 40 mm/min. Samples for chemistry analysis were taken from 1/2 radius region of the cross section of the log. Inductively coupled plasma-atomic emission spectroscopy (ICP-AES) was applied to determine the contents of Zr_s, Zr_t and Zr bound in the undissolved Zr-containing particles (Zr_p) according to the methodology described in Ref. 21. The compositions of high- and low-Zr alloy billets are shown in Table I.

Forging

The obtained billets were machined to a diameter of 350 mm for extrusion. Prior to extrusion, the billet was pre-heated to ~ 420 °C and then directly extruded to a diameter of 228 mm with a ram speed of ~ 250 mm/min. The main purpose of extrusion is to eliminate casting porosities and fragment non-metallic inclusions present in the sub-surface region of as-cast billet for forgeability improvement. The billets used for forging were sectioned from the frontmost portion at die exit of extrusion. Forging was conducted along the long axis of the extruded billet by CITIC Dicastal Co., Ltd. (Qinhuangdao, Hebei, China). Prior to forging the billet was pre-heated to ~ 400 °C, and the forging speed was ~ 7 mm/s. An obtained forged blank was sectioned along its centerline as shown in Fig. 1a. Here, the axial, radial and tangential directions of the forged blank are referred to as AD, RD and TD, respectively. Notably, the AD is nearly aligned to the forging

Table I. Chemical compositions (wt.%) of the as-cast Mg-Zn-Zr alloy billets by ICP-AES

Alloy type	Zn	Total Zr (Zr_t)	Solute Zr (Zr_s)	Zr in undissolved Zr-bearing particles (Zr_p)	Mg
High-Zr	2.98	0.67	0.64	0.03	Bal.
Low-Zr	2.84	0.43	0.38	0.05	Bal.

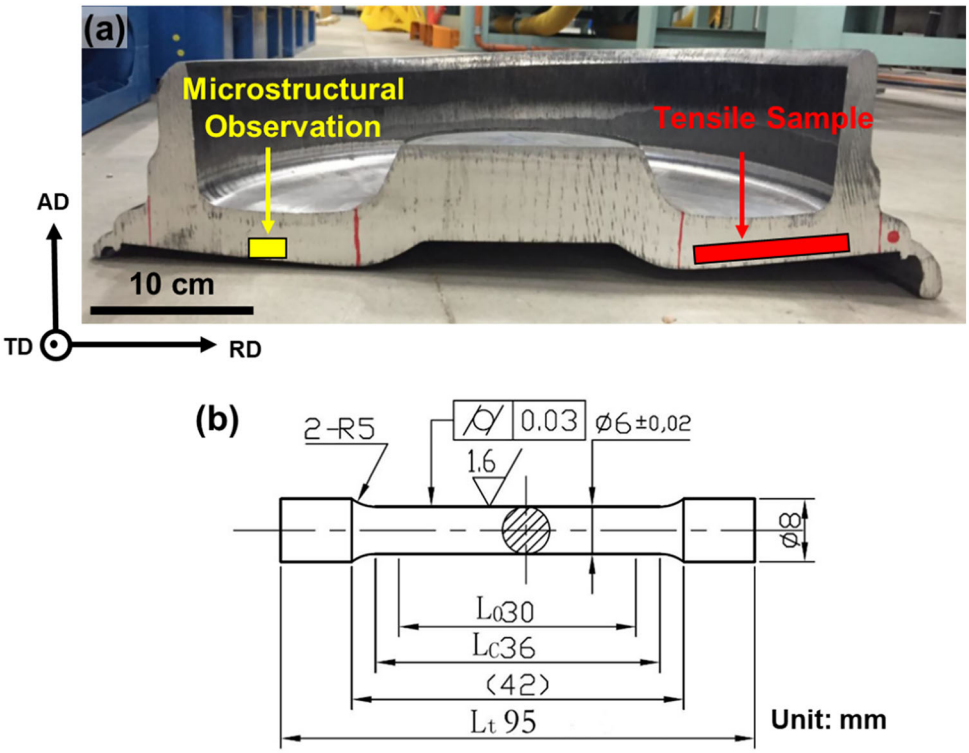

Fig. 1. (a) Sampling location for tensile testing and microstructural characterization in a forged blank; (b) tensile sample dimension.

direction, and RD and TD directions are symmetrically equivalent.

Tensile Testing

Cylindrical samples for uniaxial tensile testing were cut from the location highlighted in Fig. 1a with their long axes aligned nearly along the RD, and the detailed dimension of cylindrical samples is shown in Fig. 1b. Uniaxial tensile testing was carried out using a ZWICK/Roell Z100 (100 kN) tester at ambient temperatures with a strain rate of $\sim 1 \times 10^{-3}$ s^{-1}.

Microstructural Characterization

Optical microscopy (OM) characterization was conducted using an Olympus BX51M optical microscope, and scanning electron microscopy (SEM) characterization including energy-dispersive spectroscopy (EDS) and electron backscattering diffraction (EBSD) detections was performed using a TESCAN MIRA3 instrument equipped with an Oxford Ultim Max EDS system and Oxford C-Nano EBSD detector. EBSD datasets were processed using AZtecCrystal 2.1 software (Oxford Instruments, UK) and MATLAB R2021b (Mathworks, USA) with MTEX 5.8.1 toolbox.[35] Electron probe microanalysis (EPMA) was performed using a JEOL JXA-8530F instrument. Specimens for microscopic characterizations were all first wet ground using silicon carbide papers and then mechanically polished and ultrasonically cleaned. Samples of as-cast alloys were etched with a solution of 4 mL acetic acid, 4.4 g picric acid, 70 mL alcohol and 6 mL distilled water for OM characterization and 8 vol.% nitric acid alcohol solution for SEM and EPMA characterizations. For as-forged alloys, the samples were etched with 1 g oxalic acid, 1 mL nitric acid, 1 mL acetic acid and 150 mL distilled water for OM characterization and electrolytic polished with 4 vol.% perchloric acid alcohol solution for EBSD characterization.

Specimens for transmission electron microscopy (TEM) and scanning transmission electron microscopy (STEM) characterizations were first mechanically ground and then twinjet polished using 30 vol.% nitric acid and 70 vol.% methanol solution at an applied voltage of 20 V and a temperature of

– 30 °C. TEM and high-angle angular dark-field (HAADF) STEM imaging was performed using a FEI Talos F200S microscope operated at 200 kV.

RESULTS

As-Cast and As-Extruded Microstructures

Figure 2 shows as-cast microstructures at 1/2 radius regions of cross section of the high- and low-Zr alloy logs, respectively. Both as-cast microstructures were composed of equiaxed α-Mg grains and eutectic structures located in the inter-dendritic regions as indicated by the arrows. Eutectics was formed via binary or ternary eutectic reactions in the late stage of solidification after the nucleation and growth of primary α-Mg dendrite. Across the region of interest, the mean grain size was measured by linear intercept method to be approximately 70 ± 4 μm over 70 grains and 270 ± 4 μm over 18 grains for high- and low-Zr alloys, respectively. As-cast grain size was significantly refined by the increment in Zr content. In addition, both high- and low-Zr alloys exhibit equiaxed grain morphology. Figure 3 shows the EPMA mapping results for the as-cast microstructures of high- and low-Zr alloys. Both alloys have eutectic Mg-Zn IMCs and Zn-Zr particles located at the grain boundary region.

Zn and Zr segregations can be found in the as-cast microstructures of Mg-Zn-Zr alloys. Zn tends to segregate near the grain boundary region while Zr tends to segregate toward the grain center (Fig. 3b and e). In high-Zr alloy, most grains have a spherical Zr-rich core, and some of the Zr-rich cores have a tiny α-Zr particle embedded in the center, as highlighted in Fig. S1 (supplemental material online). These particles may be undissolved α-Zr particles released from the added Mg-Zr master alloy or alternatively primary α-Zr particles crystallized prior to α-Mg grains in the initial solidification stage. The presence of α-Zr particle in the center of α-Mg grain supports the hypothesis that the Zr-rich core is the product of a peritectic reaction (liquid + α-Zr → α-Mg).[1] According to Emley,[1] the α-Zr particle which acted as the nucleation substrate for α-Mg grain can be found only if the section happened to cut through them. In contrast, for low-Zr alloy, the distribution of Zr solute is more homogeneous. Also, no Zr-rich particle was found in the Zr-rich regions based on SEM observations, referring to Fig. S1. This indicates that the heterogeneous nucleation of α-Mg grain on the α-Zr particle was rare in the solidification of low-Zr alloy. In addition, quantitative line scans were plotted on the EPMA maps to probe Zr segregation. Figure 3c shows the Zr concentration profile along the scanning line marked in Fig. 3a. Zr content in the Zr-rich core of high-Zr alloy ranges from ~ 1% to ~ 3%. Figure 3f shows Zr concentration profile along the scanning line marked in Fig. 3d. Zr content in the Zr-rich region of low-Zr alloy ranges from ~ 1% to ~ 2%, which is substantially lower than that in the Zr-rich core of high-Zr alloy.

OM images for the as-extruded billet can be found in Supplementary Fig. S2 in which extrusion direction and radial direction are annotated as ED and RD, respectively. Grain size and grain morphology in the center and 1/2 radius regions of cross-section remained unchanged after extrusion, while grains in the near-surface region were considerably elongated as deformed by extrusion. In addition, some DRXed grains have been identified in the near-surface region of high-Zr alloy. As the billet sectioned for forging was from the frontmost of the extruded log at die exit which experienced the lowest strain during extrusion and the overall extrusion ratio is only ~ 2.4, the microstructural change induced by extrusion was minor.

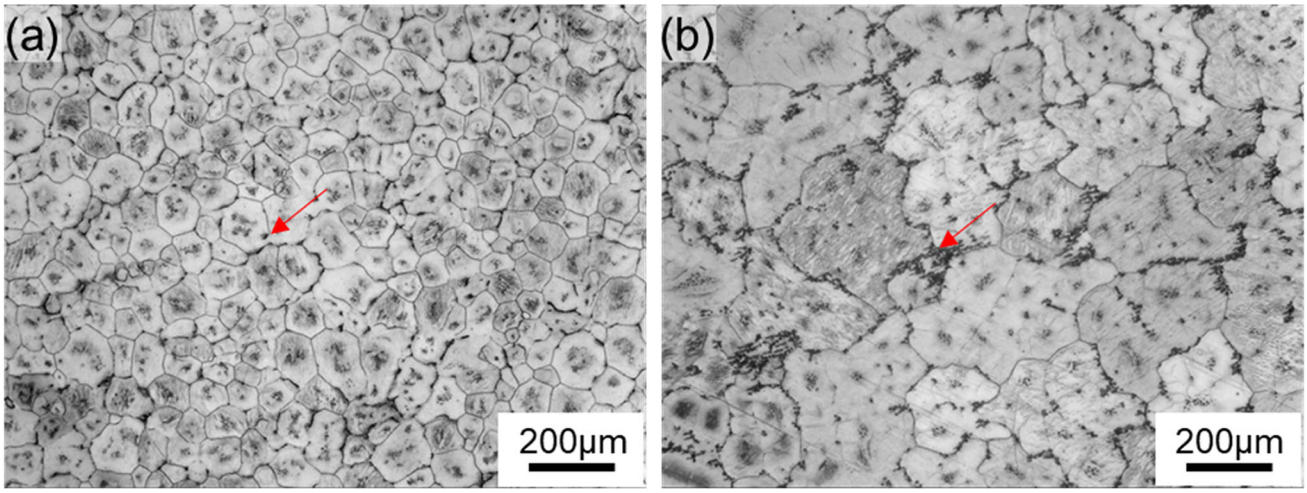

Fig. 2. Optical microscopic graphs of as-cast microstructure for (a) high-Zr and (b) low-Zr alloys (eutectic compounds of black contrast at grain boundaries are indicated by arrows).

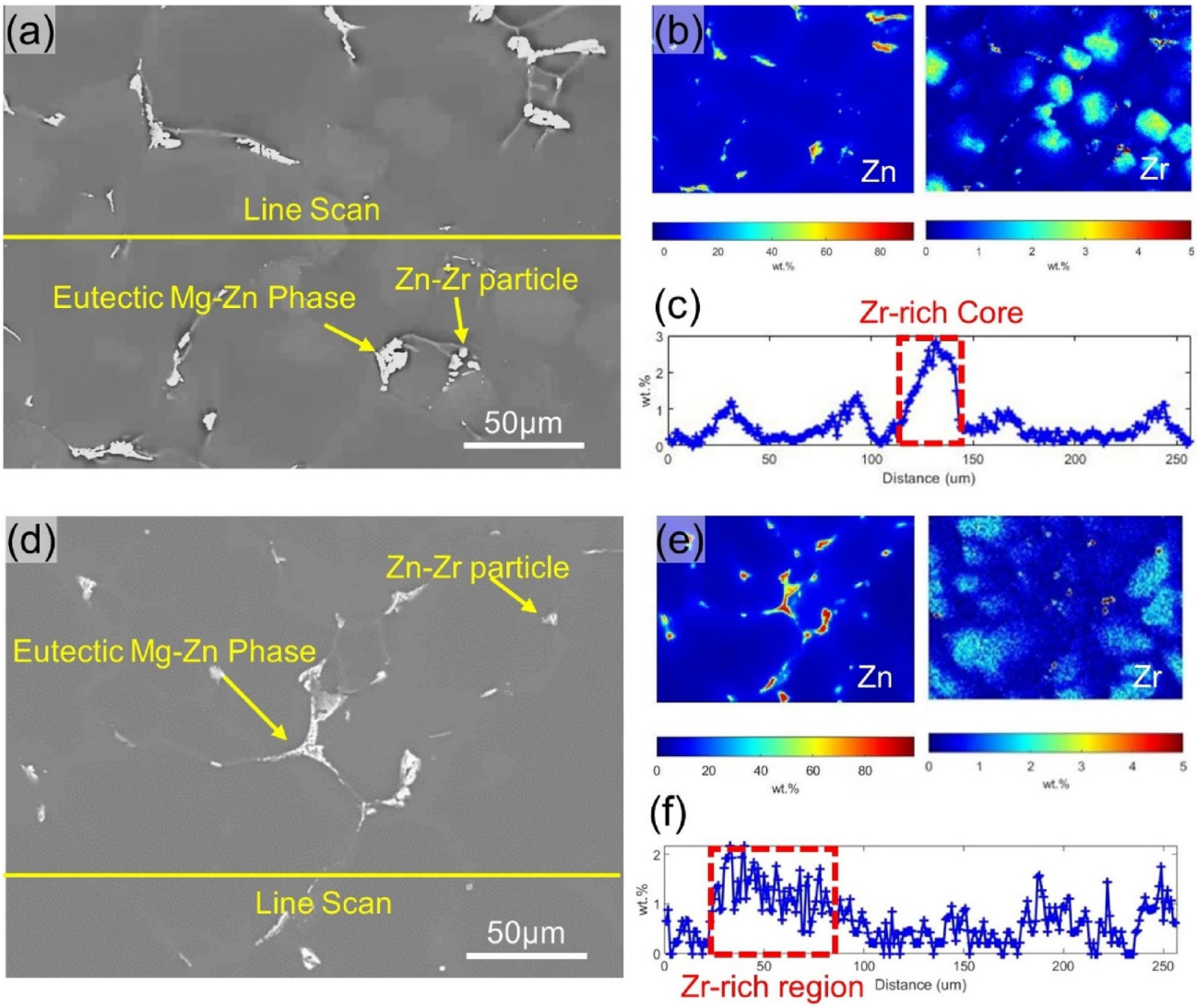

Fig. 3. EPMA results for the as-cast microstructure of (a–c) high-Zr alloy and (d–f) low-Zr alloy: (a, d) backscattered electron micrographs with the corresponding elemental maps of (b, e) Zn and Zr mapping; (c, f) quantitative line scan results of Zr and the line scan location is shown in (a) and (d).

As-Forged Microstructure

As shown in Fig. 4, the as-forged microstructures of high- and low-Zr alloys are bimodal, consisting of coarse unDRXed domains and fine DRXed grains. In high-Zr alloy, the unDRXed domains are of elliptical shape, with their long axes nearly aligned to the RD (Fig. 4a and c), while in low-Zr alloy, the unDRXed domains were considerably larger in size and of irregular morphology (Fig. 4b). As seen at a higher magnification (Fig. 4d), some unDRXed domains have been heavily elongated, yielding much larger aspect ratios. In addition, a few twin-like features of lenticular morphology can be found in some unDRXed domains as highlighted in Fig. 4f. The average DRXed grain sizes of high- and low-Zr alloys were calculated using linear intercept method (averaged over 110 grains) to be 5.1 ± 0.1 μm and 6.8 ± 0.3 μm, respectively.

EBSD measurements were performed to gain information on boundaries and grain orientations of the as-forged microstructures. Inverse pole figure (IPF) maps, superimposed with grain boundaries (GBs, misorientation $> 5°$) in black color and sub-GBs (misorientation of 2°–5°) in cyan color, are shown in Fig. 5. According to Fig. 5a and d, the overall as-forged microstructures of both high- and low-Zr alloys are strongly basal-textured with their {0001} planes nearly perpendicular to the AD (i.e. nearly perpendicular to the forging direction). According to the {0001} pole figures (PF) of Fig. 5a and d, texture intensities of the as-forged high- and low-Zr alloys are similar. In Fig. 5b and e, only DRXed grains were rendered in IPF color. The methodology applied to differentiate DRXed grains from deformed parent grains is based on the grain orientation spread (GOS) value[36,37] and grain size. Here, DRXed grain has been defined as the grain of

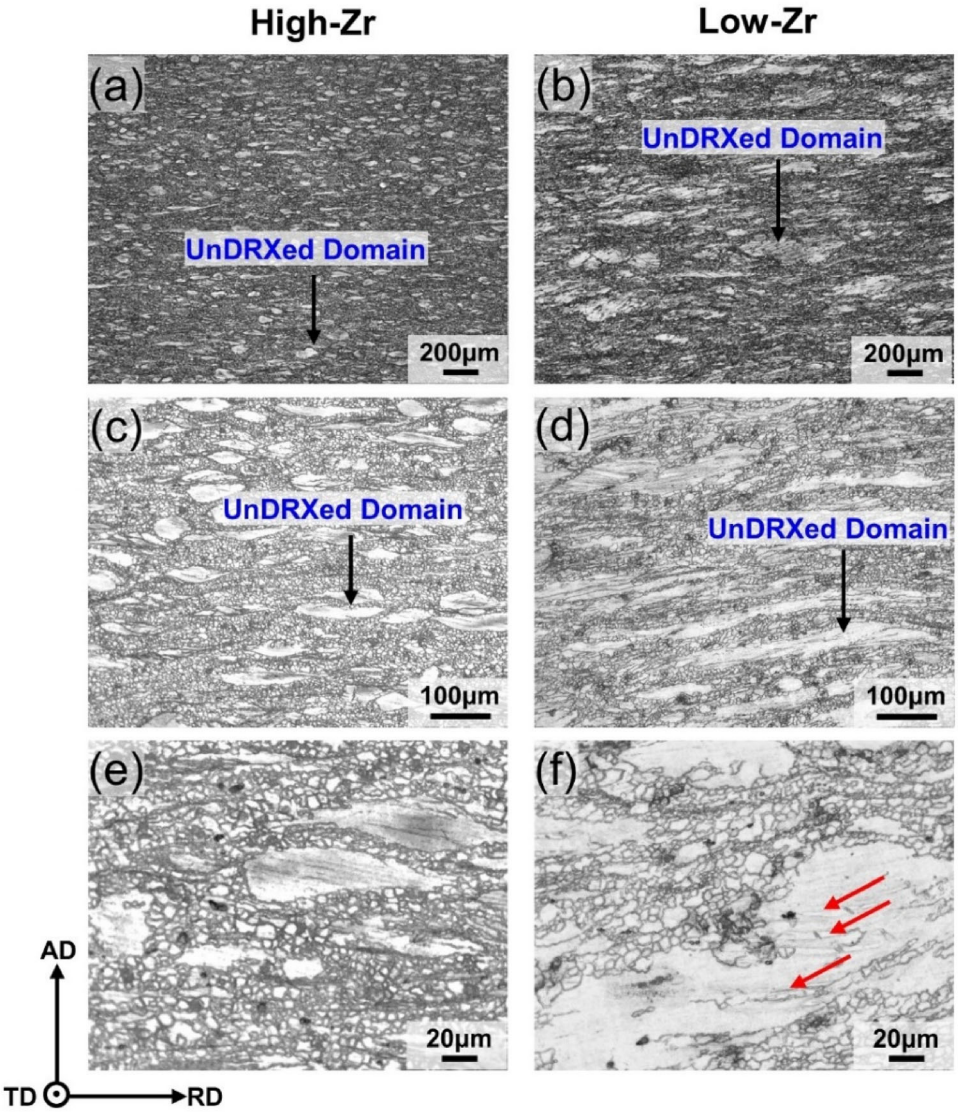

Fig. 4. Optical microscopic graphs of as-forged microstructure for high-Zr alloy (a), (c) and (e) and low-Zr alloy (b), (d) and (f). Red arrows in (f) highlight twin-like features of lenticular morphology (Color figure online).

GOS value $< 1.5°$ and equivalent diameter $< 20\ \mu$m, and the detailed reasoning for this definition is given in the authors' previous research.[26,38] The area percentages of DRXed grains are 48% and 38% for high- and low-Zr alloy, respectively. In addition, sub-GBs are mostly segregated in the unDRXed domains. Histograms of boundary misorientation distribution derived from Fig. 5a and d are plotted in Fig. 5c and f, respectively. A noticeable difference between the alloys is that a peak can be found in the misorientation range of $86° \pm 5°$ in low-Zr alloy while is absent in high-Zr alloy. This peak is probably from $\{10\bar{1}2\}$ extension twin boundary (TB) as the characteristic misorientation of extension TB is $\sim 86.3°$. This is consistent with the observation that twin-like features are present in the unDRXed domains of low-Zr alloy (Fig. 4f) while absent in the unDRXed domains of high-Zr alloy (Fig. 4e).

TEM analysis of the as-forged microstructures revealed the presence of nano-sized precipitates. For both alloys, there is a distinguishable boundary demarcating the precipitate-rich and -lean regions. Representative regions are shown in Fig. 6a and c for high- and low-Zr alloys, respectively. Figure 6b and d shows HAADF-STEM images of precipitates at a higher magnification along with the corresponding EDS mapping results. The precipitate primarily comprises Zn and Zr. The precipitation of nano-sized Zn-Zr particles has been widely reported in varied Mg-Zn-Zr-(RE) alloys containing $> 0.4\%$ Zr.[25,27,29,36–38] During homogenization heat treatment, solution heat treatment and hot forming processes (e.g. forging, extrusion), supersaturated Zr atoms in the Zr-rich cores/regions tend

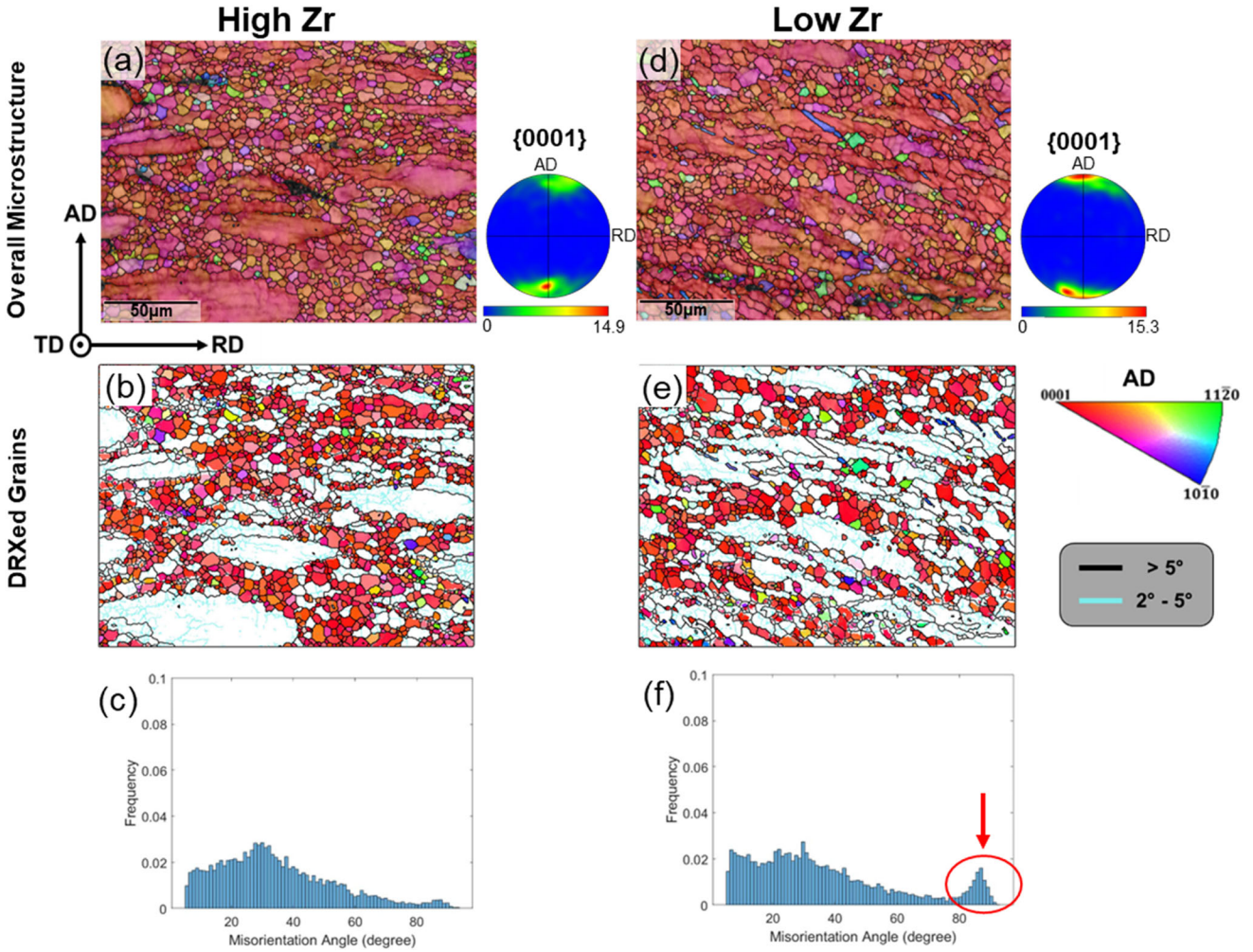

Fig. 5. IPF-AD maps (step size of 1 μm) superimposed with grain/sub-grain boundaries of the overall microstructure and DRXed portion for high-Zr alloy (a)–(b) and low-Zr alloy (d)–(e) (the corresponding {0001} PFs are also given for (a) and (d)); (c) and (f) are boundary misorientation histograms derived from (a) and (d). The portion of misorientation angles of 86° ± 5° is highlighted in (f).

to combine with Zn atoms to form Zn-Zr precipitates. In the present study, the observed Zn-Zr precipitates were likely formed in the applied extrusion and forging processes.

Notably, the observed Zn-Zr precipitates are of rod-like and polygonal morphologies in both alloys. This indicates that Zn-Zr precipitates of different chemistries and/or crystallographic structures may co-exist. A similar phenomenon has been reported by Guan et al.[41] in which the Zn_2Zr_3 phase of primitive tetragonal crystal structure and Zn_2Zr phase of face-centered cubic structure precipitated out with different morphologies in a solution heat treated Mg–5.0Sm-0.6Zn-0.5Zr (wt.%) alloy. Based on the 2D projection of Zn-Zr precipitates in the precipitate-rich region under STEM-HAADF observation, average equivalent diameter of the precipitates was calculated to be 12.9 ± 6.9 nm and 19.8 ± 10.2 nm (averaged over 700 particles) for high- and low-Zr alloys, respectively. The corresponding number density was 811 ± 215 unit/μm^2 and 565 ± 109 unit/μm^2 for high- and low-Zr alloys, respectively. Theoretically, the greater degree of supersaturation of Zr will lead to the precipitation of Zn-Zr particles of finer size and higher number density.[42]

Tensile Property and Tensile-Strained Microstructures

The as-forged Mg-Zn-Zr alloys were tensile tested quasi-statically at ambient temperature, and the corresponding engineering stress–strain curves are shown in Fig. 7a. The increased Zr addition only results in a slight increment of ~ 11.6 MPa in average 0.2% proof stress (Table II). To further understand the impact of Zr addition on strength property, elastic limits have been determined as illustrated in Fig. 7b. The average elastic limit of high-Zr alloy is ~ 9.5 MPa higher than that of low-Zr alloy (Table II). The strain hardening curves of high- and low-Zr alloys are almost overlapped, as shown in Fig. 7c, which indicates that the strain hardening capability of both alloys are comparable.

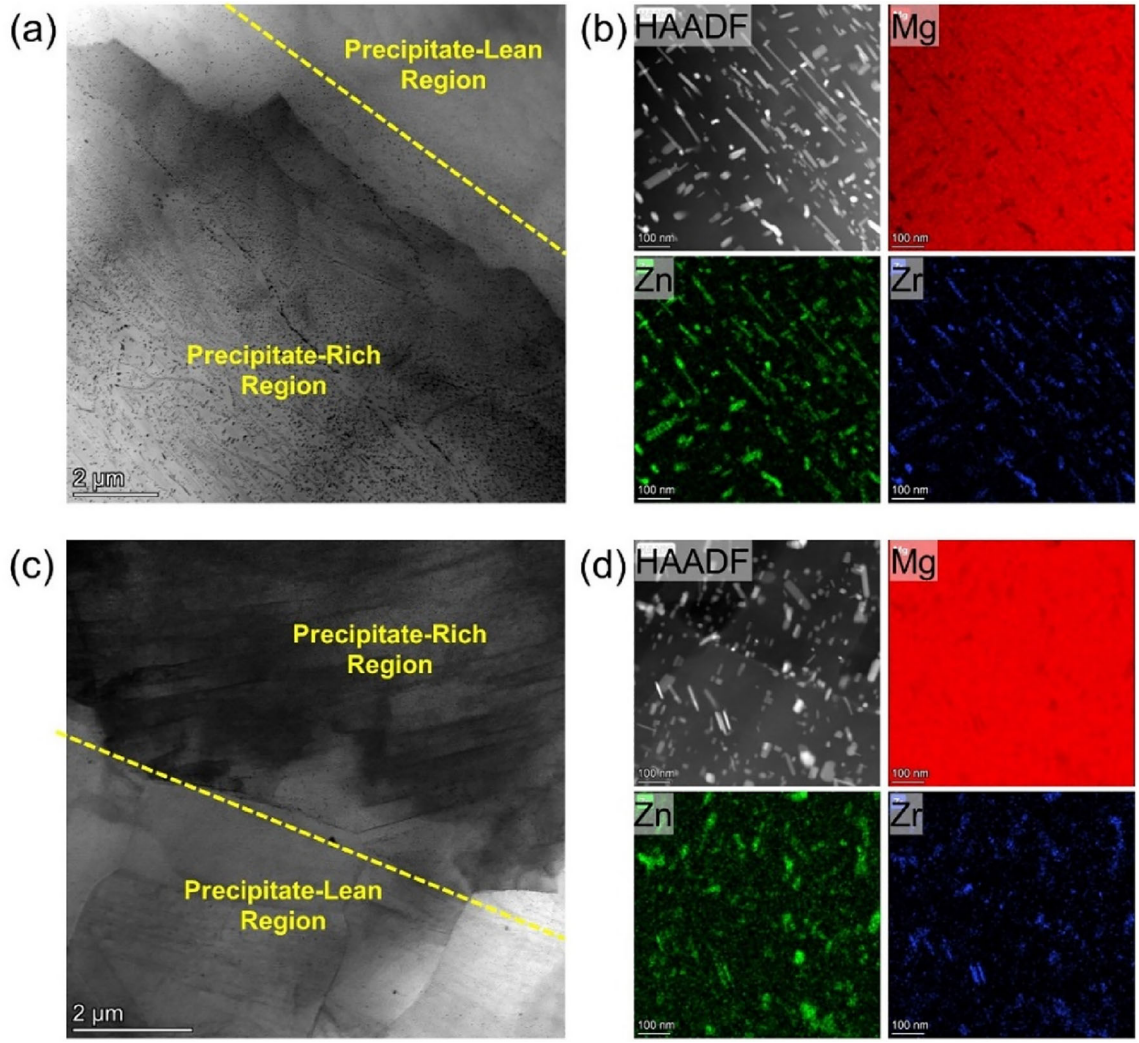

Fig. 6. TEM micrographs for the as-forged microstructure of (a-b) high-Zr and (c-d) low-Zr alloy: (a, c) bright-field images at a low magnification to show demarcation between Zr-rich region and Zr-lean region; (b, d) HAADF-STEM images of Zn-Zr precipitates with the corresponding EDS mapping results.

Hence, the difference in 0.2% proof stress between the alloys can be primarily attributed to the change in elastic limit. In addition, the increased Zr addition significantly improves tensile ductility. As shown in Table II, the uniform and post-uniform elongations of low-Zr alloy are $\sim$ 10.1% and $\sim$ 0.6%, respectively, while the counterparts of high-Zr alloy are $\sim$ 13.9% and $\sim$ 6.4%, respectively. The increment in post-uniform elongation caused by the increased Zr content is more significant.

Optical micrographs of the microstructures on the longitudinal section of the tensile-strained samples are shown in Fig. 8. For the low-Zr alloy samples tensile strained to $\sim$ 2% and $\sim$ 4%, microstructural change was minor. As the strain was increased to $\sim$ 10%, profuse twins were observed, especially within the unDRXed domains as highlighted in Fig. 8c, while for the high-Zr alloy sample tensile strained to $\sim$ 10%, only a few twins could be observed in the unDRXed domains, as highlighted in Fig. 8f. The results indicate that twinning tendency is significantly reduced with the increased Zr addition. For high-Zr alloy, a remarkable microstructural change induced by tensile straining is that the aspect ratio of unDRXed domains becomes larger with the long axes aligned to the tensile axis. Microstructures near the fractured surfaces of the tensile-to-fracture samples were also checked by OM, as shown in Fig. 9. For both alloys, twins not only formed in unDRXed domains but also in DRXed grains. Furthermore, profuse twin cluster and twin-twin intersections can be found near the fractured surfaces or long cracks, as highlighted in Fig. 9.

The widely reported twinning systems in Mg alloys are $\{10\bar{1}2\}$ extension twinning and $\{10\bar{1}1\}$ compression twinning. The former tends to be activated when loading geometrically favors tension along the c-axes of grains,[39] and the latter operates when grains are deformed in compression along

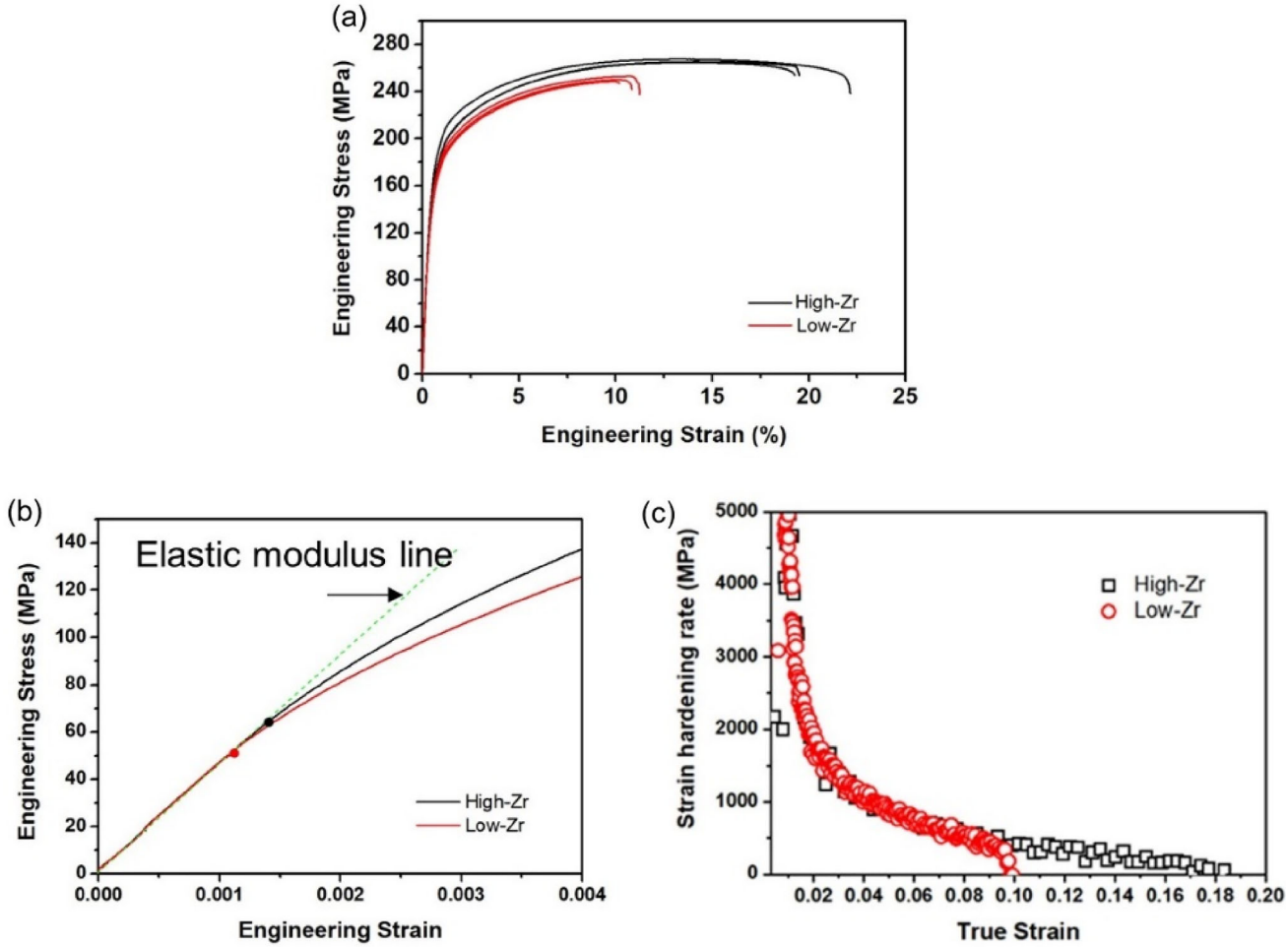

Fig. 7. Uniaxial tensile properties of the Mg-Zn-Zr alloys: (a) engineering stress–strain curves, (b) determination of elastic limits, (c) strain hardening rate curves.

Table II. Uniaxial tensile property of as-forged Mg-Zn-Zr alloys

	High-Zr alloy	Low-Zr alloy
Elastic limit (MPa)	58.8 ± 0.6	49.3 ± 2.3
0.2% Proof stress (MPa)	158.3 ± 6.7	146.7 ± 5.5
Ultimate tensile stress (MPa)	265.7 ± 1.2	250.3 ± 2.5
Uniform elongation (%)	13.9 ± 0.4	10.1 ± 0.5
Post-uniform elongation (%)	6.4 ± 1.9	0.6 ± 0.3
Elongation to fracture (%)	20.3 ± 1.6	10.7 ± 0.5

their c-axes.[40,41] In addition, a secondary extension twin may nucleate inside a compression twin to form $\{10\bar{1}1\}$-$\{10\bar{1}2\}$ double twins. The twins formed in the region near the fractured surface of a low-Zr alloy sample were identified via EBSD characterization based on angle/axis relationship of boundaries,[42] as shown in Fig. 10. Most of the twins were indexed as extension type. Notably, the matrix is of typical basal orientation with the c-axes of most grains nearly perpendicular to the tensile axis. Under this condition, the activation of extension twinning was not favored because of the unidirectional nature of the twinning mechanism. Ando et al.[43,44] observed similar anomalous activation of extension twinning during the tensile deformation of a basal-textured AZ31 Mg sheet when the loading direction did not favor extension twinning. It was explained that the anomalous extension twinning was activated to relax strain incompatibility between the neighboring grains rather than to accommodate the plastic strain incurred by external loading. It is interesting that though the tensile loading parallel to basal plane geometrically favors the activation of compression twinning, only a

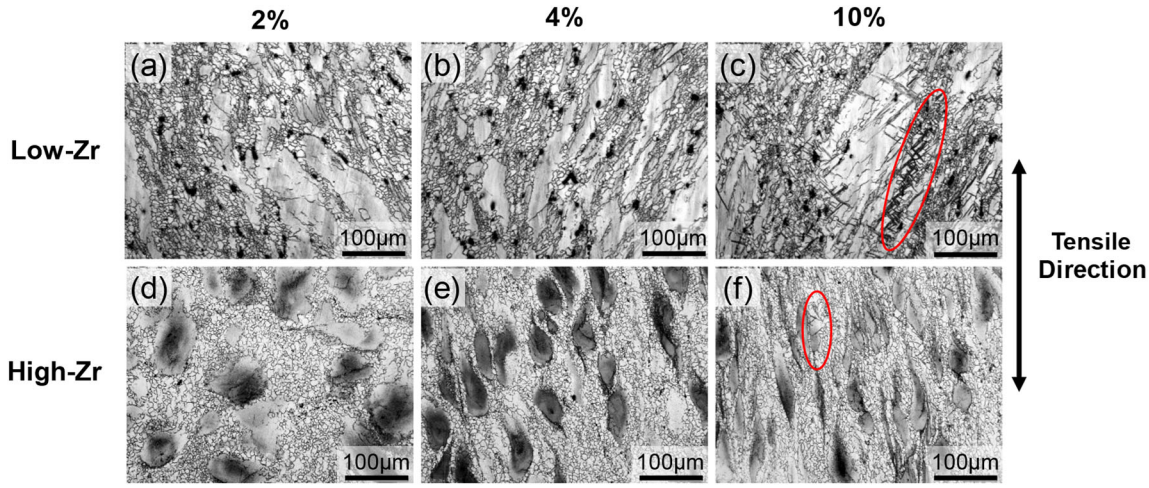

Fig. 8. Optical microscopic graphs of tensile tested microstructure for high-Zr (a)–(c) and low-Zr alloys (d)–(f). Varied engineering strains were obtained including 2% (a) and (d), 4% (b) and (e) and 10% (c) and (f). The microstructures are observed on the longitudinal section of middle region in the gauge length of tested samples. Clusters of twin-like features are highlighted in (c) and (f).

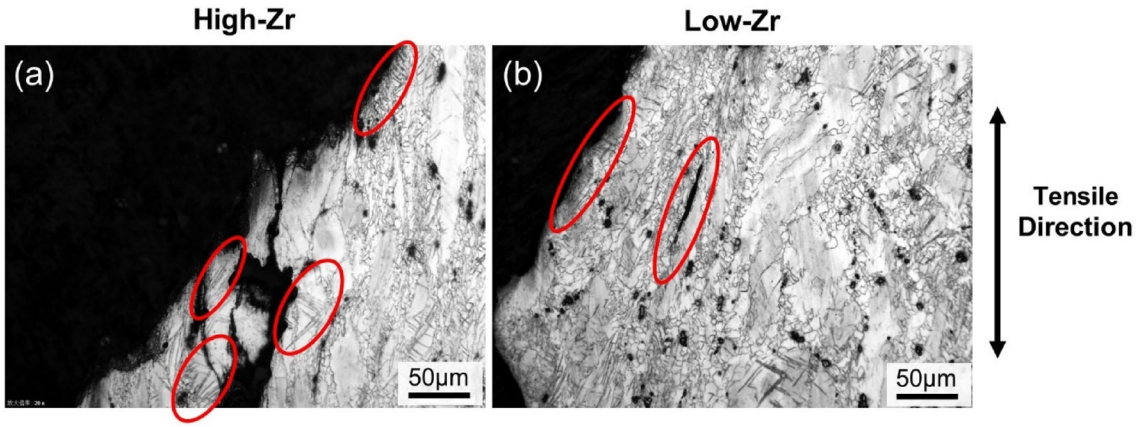

Fig. 9. Optical microscopic graphs of the microstructures near the fractured surfaces of (a) high-Zr alloy and (b) low-Zr alloy. Twin clusters near the fractured surface and long cracks were highlighted.

limited fraction of compression twins was observed, and double twin was absent in the fractured samples. A potential explanation is that the plastic strain has been localized at the sites of compression and double twins,[45–48] which retarded an accurate indexing of these twin boundaries in EBSD analysis.

DISCUSSION

Effects of Zr Addition on Microstructural Evolution

The present study revealed that the microstructure evolution of Mg-Zn-Zr alloys during casting and forging was affected by Zr addition levels. Chemical analysis results shown in Table I indicate that undissolved Zr-containing particles were present in both high- and low-Zr alloys. The undissolved Zr-containing particles can be categorized into three types: (1) α-Zr particles inherited from the added Mg-Zr master alloy which were not completely dissolved prior to casting;[18] (2) primary α-Zr particles nucleated from the melt, owing to the reduced solubility of Zr in the molten Mg with decreased temperature; (3) Zn-Zr intermetallic particles formed via eutectic reactions and located within inter-dendritic regions (Fig. 3 and Fig. S1). An equilibrium Mg-Zr binary phase diagram plotted using Pandat software with PanMg2021 database is shown in Fig. S3. It is predicted that the solubility of Zr in liquid Mg at the peritectic temperature (~ 654 °C) is ~ 0.57%. In the previous research, solubility of Zr in liquid Mg at the peritectic temperature is reported as only 0.45%[49] or 0.50%.[5] Since Zr_s of high- and low-Zr alloy was measured to be 0.64% and 0.38%, respectively, in situ formed α-Zr particles would probably be present in the casting of high-Zr alloy while be absent in the casting of low-Zr alloy.

For high-Zr alloy, Zr_s is higher than the solubility of Zr at the peritectic temperature and α-Zr particles suspended in the melt would participate into the

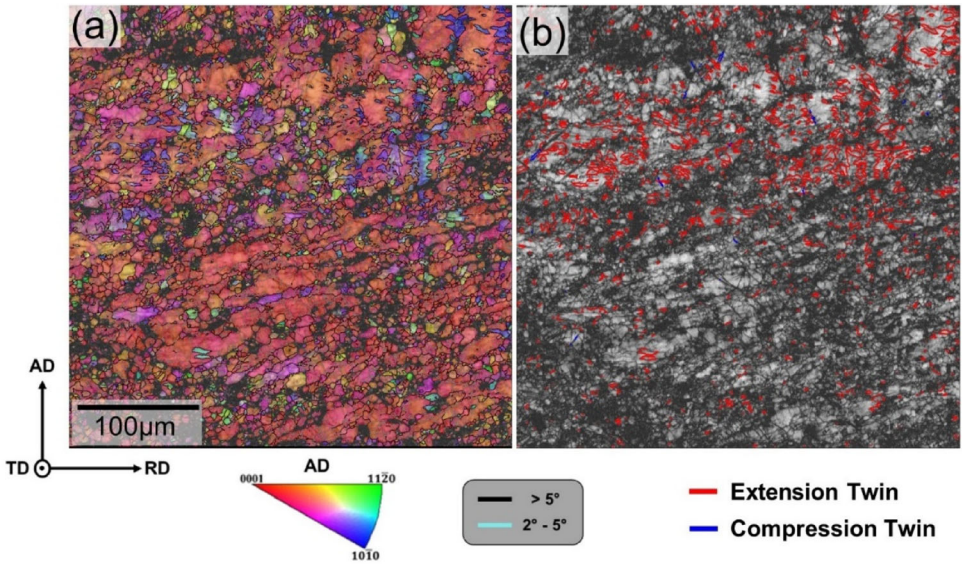

Fig. 10. (a) IPF-AD map (step size of 0.5 μm) superimposed with grain/sub-grain boundaries and (b) band contrast map superimposed with twin boundaries of as-forged low-Zr alloy strained to fracture.

peritectic reaction (liquid + α-Zr → α-Mg) to form Zr-rich coring structures in the resulting as-cast microstructure, while for low-Zr alloy, the peritectic reaction was unlikely to occur because of the insufficient Zr_s content, though undissolved α-Zr particles may have existed in the melt. Therefore, the observed Zr-rich regions in the as-cast microstructure of low-Zr alloy mainly resulted from solute segregation at the solidification front. Consequently, Zr content in the Zr-rich regions of low-Zr alloy is lower compared to that in the Zr-rich cores of high-Zr alloy.

Another important impact from the lower Zr_s and the absence of the peritectic reaction is that the as-cast grain size of low-Zr alloy is much coarser (Fig. 2), which may affect the size distribution of unDRXed domains in the as-forged microstructures. The morphology and size distribution of the unDRXed domains in the as-forged microstructure of high-Zr alloy (Fig. 4c) are similar to the Zr-rich coring structures observed in its as-cast microstructure (Fig. 3b). It is inferred that the formation of unDRXed domains in high-Zr alloy mainly resulted from Zenner pinning effect exerted by the Zn-Zr particles precipitated in the Zr-rich cores on the movement of dislocations and sub-GBs.[27,31] In contrast, the size of unDRXed domains present in the as-forged microstructure of low-Zr alloy (Fig. 4d) is substantially larger than the Zr-rich regions in its as-cast microstructure (Fig. 3d). This implies that the precipitation of Zn-Zr particles is not the deterministic factor for the formation of unDRXed domains in low-Zr alloy. Conventionally, DRX initiates at the grain boundary region via grain boundary bulging mechanism and gradually spreads to the grain interior to consume the whole grain. A more likely explanation for the formation of large-sized unDRXed domains in low-Zr alloy is that DRX kinetics under the present forging condition was insufficient to consume the initial coarse-grained microstructure.

According to Fig. 8, the as-forged high-Zr alloy exhibited a suppressed twinning activity compared to the as-forged low-Zr alloy. The intrinsic microstructural features affecting the twinning tendency mainly include grain orientation, grain size and precipitated particles in the grain interior. According to the EBSD results shown in Fig. 5, both alloys show basal-textured microstructures which do not favor the activation of extension twinning in the uniaxial tensile test conducted in the present study. Hence, the influence of grain orientations can be ruled out. It has been widely reported that smaller grain size yields a higher twin-interface energy resulting in a higher CRSS value for the activation of twinning.[12,50–53] Both the unDRXed domains and DRXed grains of high-Zr alloy are more refined than the counterparts of low-Zr alloy, which may result in the reduced twinning tendency. In addition, it has been reported that finely dispersed precipitates contributed to the suppression of mechanical twinning in the coarse unDRXed domains of Mg alloys.[31,54] As mentioned above, the unDRXed domains of high-Zr alloy showed very good correlation with the initial Zr-rich coring structures in the as-cast microstructure whereas the unDRXed domains of low-Zr alloy were much larger than the initial Zr-rich regions in the as-cast microstructure. Hence, the unDRXed domains of high-Zr alloy are expected to be occupied by Zn-Zr precipitates with a high number density in a more homogeneous distribution manner. This may also contribute to the reduced twinning tendency of high-Zr alloy.

Effects of As-Forged Microstructure on Tensile Property

The main deformation mechanisms in Mg and its alloys include dislocation slip and mechanical twinning. The most frequently activated slip systems in room-temperature deformation include $\{0001\}<11\bar{2}0>$ basal slip and $\{10\bar{1}0\}<11\bar{2}0>$ prismatic slip. For the twinning systems of Mg alloys, $\{10\bar{1}2\}$ extension twinning has a relatively low critical resolved shear stress (CRSS) value and tends to be activated when loading direction favors tension along the c-axes of grains,[39] while $\{10\bar{1}1\}$ compression twinning operates when grains are deformed in compression along the c-axes.[40,41] Due to a very high CRSS value of $\{10\bar{1}1\}$ compression twinning,[55] compression twins were less frequently observed under room-temperature deformation. According to the OM characterizations of the Mg-Zn-Zr alloys at varied tensile strain levels (Fig. 8), the density of twins did not increase in the incipient deformation stage of tensile strain < 4% compared to the initial as-forged microstructures (Fig. 4). It is inferred that twinning is not the dominant deformation mechanism in this stage. This is consistent with the results of previous studies[12,44,56,57] in which tensile tests were conducted on the as-extruded and as-rolled Mg alloys with the tensile axis nearly perpendicular to the c-axes of α-Mg grains. Hence, it is speculated that the deformation mechanism responsible for macro-yielding of the Mg-Zn-Zr alloys was dislocation slip. In general, a stronger basal texture[39,58] will increase the stress required to activate basal slip when the loading tends to compress along the basal poles. In addition, CRSS of basal slip tends to increase with decreasing grain size.[59,60] Since the texture of the two as-forged alloys are similar (Fig. 5), the slightly higher elastic limit of the as-forged high-Zr alloy (Table II) could be mainly attributed to the effect of microstructure refinement (Fig. 4).

The higher uniform elongation of the as-forged high-Zr alloy needs to be analyzed from multiple aspects. Previous research reported that texture has a strong correlation with uniform elongation of Mg alloys.[58,61] The underlying mechanism is that strain hardening rate will be enhanced when profuse extension twinning can be activated in the early stage of deformation. Referring to Figs. 7 and 8, it is obvious that twin-induced strain hardening is absent in the tensile deformation of the as-forged high-Zr alloy. In another aspect, a work conducted by Barnett[45] built a correlation between the flow localization induced by double twins and decreased uniform elongation. It has been well accepted that plastic strain accommodated by basal slip will be localized within double twins formed in the basal-oriented Mg matrix leading to stress concentration and subsequently initiation of cracks at the twin boundaries.[44] Hence, the suppressed twinning behavior in the as-forged high-Zr alloy may contribute to the higher uniform elongation.

As for post-uniform elongation, it has been widely reported that grain size plays a deterministic role in the tensile deformation of basal-textured Mg alloys.[58,61–63] It was interpreted that decreased grain size enhanced dynamic recovery in the late stage of deformation, which improved post-uniform elongation.[63,64] As aforementioned in Sect. "Tensile Property and Tensile-Strained Microstructures", extension twinning is responsible for releasing stress concentrations at grain boundaries. When extension twinning is suppressed in the fine-grained microstructure, non-basal slip activity may be enhanced because of the unrelaxed stress concentrations at grain boundaries. The activation of non-basal slip systems contributes to increased dynamic recovery and improved post-uniform elongation. This is consistent with our observation that the formation of profuse extension twins was significantly delayed in the as-forged high-Zr alloy during tensile deformations (Fig. 8) with a much larger post-uniform elongation relative to the as-forged low-Zr alloy.

In a summary, increasing Zr addition from ~ 0.43% to ~ 0.67% has a minor impact on 0.2% proof stress but remarkably improves tensile ductility. If high ductility (> 20%) is required for a forged Mg-Zn-Zr product, it is suggested to add Mg-Zr master alloy to an amount where the solute Zr content in the molten Mg exceeds the solubility of Zr at the peritectic temperature. If strength is the sole critical property, a lower total Zr content of ~ 0.4% may be desirable, which can help save cost via reducing the dosage of Mg-Zr master alloy. In addition, the relatively lower twinning tendency of High-Zr alloy may be beneficial for fatigue durability and fracture toughness, which warrants further investigations.

CONCLUSION

In the present study, Mg-Zn-Zr alloys with two levels of Zr addition (Mg-3%Zn-0.43%Zr and Mg-3%Zn-0.67%Zr) were prepared. Systematic characterizations have been conducted on as-cast, as-forged and tensile-strained microstructures of the Mg-Zn-Zr alloys to understand their microstructure-property relationship as affected by varied levels of Zr addition. The following conclusions can be drawn:

1. With the total Zr addition increasing from 0.43% to 0.67%, solute Zr content significantly increased from 0.38% to 0.64%, which activated the α-Zr particles suspended in the molten Mg to nucleate α-Mg grains in a peritectic reaction (liquid + α-Zr → α-Mg). As a result, grain size has been refined from ~ 260 μm to ~ 70 μm. In addition, Zr-rich coring structures were present in Mg-3%Zn-0.67%Zr alloy while absent in Mg-

3%Zn-0.43%Zr alloy. For Mg-3%Zn-0.43%Zr alloy, Zr-rich regions can be observed in the as-cast microstructure due to the partitioning of Zr solute at liquid–solid interphase in solidification. Zr supersaturation in the Zr-rich regions of Mg-3%Zn-0.43%Zr alloy is lower than that in the Zr-rich coring structures of Mg-3%Zn-0.67%Zr alloy.

2. Subjected to the forging process, both alloys exhibit basal-textured bimodal microstructures comprising coarse unDRXed domains and fine DRXed grains. Both unDRXed domains and DRXed grains became more refined with the increased Zr content. The formation mechanism of unDRXed domains in the Mg-Zn-Zr alloys is potentially different. For Mg-3%Zn-0.67%Zr alloy, unDRXed domains in the as-forged microstructure inherited initial Zr-rich coring structures in the as-cast microstructure, caused by the pinning effect of precipitated Zn-Zr particles exerted on the movement of dislocations and subgrain boundaries. In contrast, the formation of unDRXed domains of Mg-3%Zn-0.43%Zr alloy is probably because that DRX kinetics under the present forging condition was insufficient to consume the initial coarse-grained microstructure.
3. Increasing Zr addition from $\sim$ 0.43% to $\sim$ 0.67% has a minor impact on 0.2% proof stress but remarkably improves tensile ductility. Both uniform and post-uniform elongations became larger with the increased Zr content, which likely resulted from the suppressed twinning tendency incurred by refined microstructure and a high number density of Zn-Zr particles which homogeneously precipitated in the unDRXed domains.

SUPPLEMENTARY INFORMATION

The online version contains supplementary material available at https://doi.org/10.1007/s11837-023-05902-7.

ACKNOWLEDGEMENTS

The authors acknowledge the experimental assistance from Mr. Jinlong Zhu from GM China Science Lab. G.Z. acknowledges the funding from National Natural Science Foundation of China (51904352), and Scientific Research Foundation of Hunan Provincial Education Department, China (22A0004). W. Sun is grateful for the Fundamental Research Funds for the Central Universities of Central South University.

DATA AVAILABILITY

The raw/processed data required to obtain these results can be shared upon reasonable request to the corresponding author.

CONFLICT OF INTEREST

The authors declare that they have no known competing financial interests or personal relationships that could influence this work.

REFERENCES

1. E.F. Emley, *Principles of Magnesium Technology* (Pergamon Press, Oxford, 1966).
2. Y. Lee, A. Dahle, and D. StJohn, *Metall. Mater. Trans. A* 31, 2895 (2000).
3. Y. Tamura, N. Kono, T. Motegi, and E. Sato, *Keikinzoku* 47, 679 (1997).
4. M. Sun, M.A. Easton, D.H. StJohn, G. Wu, T.B. Abbott, and W. Ding, *Adv. Eng. Mater.* 15, 373 (2013).
5. H.E. Friedrich, and B.L. Mordike, *Magnesium technology* (Springer, 2006).
6. A.I.H. Committee, *ASM Int.* 2, 1143 (1992).
7. X. Lin, L. Tan, Q. Zhang, K. Yang, Z. Hu, J. Qiu, and Y. Cai, *Acta Biomater.* 9, 8631 (2013).
8. S. Karparvarfard, S.K. Shaha, S.B. Behravesh, H. Jahed, and B.W. Williams, *J. Mater. Sci. Technol.* 33, 907 (2017).
9. M. Alvarez-Leal, A. Orozco-Caballero, F. Carreño, and O.A. Ruano, *Mater. Sci. Eng. A* 710, 240 (2018).
10. G. Govind, K. Nair, M. Mittal, R. Sikand, and A. Gupta, *Mater. Sci. Technol.* 24, 399 (2008).
11. M. Carsí, F. Carreño, and O.A. Ruano, *Materials science forum* (Trans Tech Publication, 2018), pp2325–2330.
12. A. Malik, Y. Wang, F. Nazeer, M.A. Khan, M. Sajid, S. Jamal, and W. Mingjun, *J. Alloy. Compd.* 858, 157740 (2021).
13. S. Karparvarfard, S. Shaha, S. Behravesh, H. Jahed, and B. Williams, *MATEC web of conferences* (EDP Sciences, 2018), p06009.
14. G. Popescu, P. Moldovan, D. Bojin, and W.H. Sillekens, *Univ. Politeh. Buchar. Sci. Bull. Ser. B Chem. Mater. Sci.* 71, 85 (2009).
15. A. Dziubińska, A. Gontarz, M. Dziubiński, and M. Barszcz, *Adv. Sci. Technol. Res. J.* 10, 31 (2016).
16. B. Nagasivamuni, G. Wang, D.H. StJohn, and M.S. Dargusch, *J. Cryst. Growth* 512, 20 (2019).
17. X. Tong, G. Wu, M.A. Easton, M. Sun, D.H. StJohn, R. Jiang, and F. Qi, *Scr. Mater.* 215, 114700 (2022).
18. M. Qian, L. Zheng, D. Graham, M. Frost, and D. StJohn, *J. Light Met.* 1, 157–165 (2001).
19. P. Sasha, and S. Viswanathan, *Trans. Am. Found. Soc.* 119, 469 (2011).
20. M. Qian, Z. Hildebrand, and D. StJohn, *Metall. Mater. Trans. A* 40, 2470 (2009).
21. M. Qian, D.H. StJohn, and M.T. Frost, *Materials science forum* (Trans Tech Publication, Zurich-Uetikon, 2003), pp593–598.
22. B. Mordike, *Mater. Sci. Eng. A* 324, 103 (2002).
23. M. Qian, D. StJohn, and M. Frost, *Scr. Mater.* 46, 649 (2002).
24. M. Qian, and D.H. StJohn, *Int. J. Cast Met. Res.* 22, 256 (2009).
25. J. Robson, and C. Paa-Rai, *Acta Mater.* 95, 10 (2015).
26. J. You, Y. Huang, C. Liu, H. Zhan, L. Huang, and G. Zeng, *Materials* 13, 2348 (2020).
27. A. Hadadzadeh, F. Mokdad, B.S. Amirkhiz, M. Wells, B.W. Williams, and D.L. Chen, *Mater. Sci. Eng. A* 724, 421 (2018).
28. K. Huang, and R.E. Logé, *Mater. Des.* 111, 548 (2016).

29. T. Bhattacharjee, T. Sasaki, B. Suh, T. Nakata, S. Kamado, N. Kim, and K. Hono, *Magnesium technology 2015* (Springer, 2015), pp209–213.
30. A. Hadadzadeh, F. Mokdad, M. Wells, and D. Chen, *Mater. Sci. Eng. A* 709, 285 (2018).
31. K. Oh-Ishi, C. Mendis, T. Homma, S. Kamado, T. Ohkubo, and K. Hono, *Acta Mater.* 57, 5593 (2009).
32. T. Bhattacharjee, T. Nakata, T. Sasaki, S. Kamado, and K. Hono, *Scr. Mater.* 90, 37 (2014).
33. J. Da Silva Rodrigues, L.M. Antonini, A.A. Da Cunha Bastos, J. Zhou, and C. De Fraga Malfatti, *Surf. Coat. Technol.* 410, 126983 (2021).
34. J.F. Chinella, CCDC army research laboratory Aberdeen proving ground United States (2020).
35. F. Bachmann, R. Hielscher, and H. Schaeben, *Solid state phenomena* (Trans Tech Publication, 2010), pp63–68.
36. J. Li, J. Barrirero, G. Sha, H. Aboulfadl, F. Mücklich, and P. Schumacher, *Acta Mater.* 108, 207 (2016).
37. W. Wang, D. Wu, R. Chen, Y. Qi, H. Ye, and Z. Yang, *J. Alloy. Compd.* 832, 155016 (2020).
38. K. Guan, B. Li, Q. Yang, D. Zhang, X. Zhang, J. Zhang, L. Zhao, X. Liu, and J. Meng, *Mater. Charact.* 145, 329–336 (2018).
39. X.-L. Nan, H.-Y. Wang, L. Zhang, J.-B. Li, and Q.-C. Jiang, *Scr. Mater.* 67, 443 (2012).
40. D. Sun, and C. Chang, *Mater. Sci. Eng. A* 603, 30 (2014).
41. H. Kim, J.-H. Lee, C. Lee, W. Bang, S. Ahn, and Y. Chang, *Mater. Sci. Eng. A* 558, 431 (2012).
42. M. Vaughan, W. Nasim, E. Dogan, J. Herrington, G. Proust, A. Benzerga, and I. Karaman, *Acta Mater.* 168, 448 (2019).
43. J. Koike, Y. Sato, D. Ando, *Materials transactions*, 0811070603–0811070603 (2008).
44. D. Ando, J. Koike, and Y. Sutou, *Mater. Sci. Eng. A* 600, 145 (2014).
45. M. Barnett, *Mater. Sci. Eng. A* 464, 8 (2007).
46. J. Koike, *Metall. Mater. Trans. A.* 36, 1689 (2005).
47. A. Jain, O. Duygulu, D. Brown, C. Tomé, and S. Agnew, *Mater. Sci. Eng. A* 486, 545 (2008).
48. P. Cizek, and M. Barnett, *Scr. Mater.* 59, 959 (2008).
49. M. Hämäläinen, and K. Zeng, *Calphad* 22, 375 (1998).
50. M.A. Kumar, and I.J. Beyerlein, *Mater. Sci. Eng. A* 771, 138644 (2020).
51. M. Tsai, and C. Chang, *Mater. Sci. Technol.* 29, 759 (2013).
52. B. Li, S.P. Joshi, O. Almagri, Q. Ma, K. Ramesh, and T. Mukai, *Acta Mater.* 60, 1818 (2012).
53. H. Asgari, A. Odeshi, J. Szpunar, L. Zeng, and E. Olsson, *Mater. Charact.* 106, 359 (2015).
54. T. Homma, C. Mendis, K. Hono, and S. Kamado, *Mater. Sci. Eng., A* 527, 2356 (2010).
55. A. Chapuis, and J.H. Driver, *Acta Mater.* 59, 1986 (2011).
56. B. Wang, D. Xu, L. Sheng, E. Han, and J. Sun, *J. Mater. Sci. Technol.* 35, 2423 (2019).
57. C. Xu, G. Fan, T. Nakata, X. Liang, Y. Chi, X. Qiao, G. Cao, T. Zhang, M. Huang, and K. Miao, *Metall. Mater. Trans. A.* 49, 1931 (2018).
58. X. Huang, K. Suzuki, A. Watazu, I. Shigematsu, and N. Saito, *Mater. Sci. Eng. A* 488, 214 (2008).
59. P. Dobroň, F. Chmelík, S. Yi, K. Parfenenko, D. Letzig, and J. Bohlen, *Scr. Mater.* 65, 424 (2011).
60. H. Fan, S. Aubry, A. Arsenlis, and J.A. El-Awady, *Scr. Mater.* 112, 50 (2016).
61. M. Jiang, C. Xu, T. Nakata, H. Yan, R. Chen, and S. Kamado, *Mater. Sci. Eng. A* 678, 329 (2016).
62. H. Watanabe, *J. Mater. Eng. Perform.* 22, 3450 (2013).
63. B. Shi, R. Chen, W. Ke, and J. Magnes, *Alloys* 1, 210 (2013).
64. Q. Yang, and A. Ghosh, *Acta Mater.* 54, 5159 (2006).